INSTITUTE OF PHYSICS PUBLISHING PHYSICS IN MEDICINE AND BIOLOGY

Phys. Med. Biol. **51** (2006) 5859–5873 doi:10.1088/0031-9155/51/22/009

A model to simulate tumour oxygenation and dynamic [18F]-Fmiso PET data

Catherine J Kelly and Michael Brady

Wolfson Medical Vision Laboratory, Information Engineering, University of Oxford, Parks Road, OX1 3PJ, UK

E-mail: ckelly@robots.ox.ac.uk

Received 15 March 2006, in final form 2 October 2006
Published 27 October 2006
Online at stacks.iop.org/PMB/51/5859

Abstract

The microenvironment of a tumour, in particular its hypoxic status, is a crucial factor in its response to radiotherapy. Conventional techniques for measuring hypoxia are either invasive or follow surgical intervention, and thus not ideal. Positron emission tomography allows the non-invasive pre-surgical assessment of oxygen status by measuring the spatiotemporal distribution of hypoxia-specific tracers. However, the relationship between levels of uptake and the underlying oxygen tension are yet to be elucidated. Furthermore, it is not fully understood how changes in the underlying physiology affect the appearance of uptake. This paper presents a modular simulation of the tumour microenvironment, underpinned by a probability density function (PDF) to model the vasculature. The model is solved numerically, to simulate both the steady-state oxygenation of a tumour and the spatiotemporal distribution of the hypoxia-specific tracer, [18F]-fluoromisonidazole (Fmiso), in a 2D environment. The results show that using a PDF to represent the vasculature effectively captures the 'hypoxic island' appearance of oxygen-deficient tissues seen *ex vivo*. Simulated tissue activity curves (TACs) demonstrate the general two-stage trend of empirical data, with an initial perfusion-dominated uptake, followed by hypoxia-specific binding. In well-perfused tissue, activity follows plasma levels in early stages, with binding of Fmiso only becoming apparent at a later stage. In structurally hypoxic tissue, a more gradual initial increase in activity is observed, followed by the same accumulation slope. We demonstrate the utility of theoretical modelling of tracer uptake, by quantifying the changes in TAC structure that arise as a result of altering key physiological characteristics. For example, by decreasing either the proximity of tissue to the vasculature, or the effective diffusion coefficient of Fmiso, we can observe a shift of TAC structure from corresponding to well-perfused to avascular regions, despite wholly different underlying causes.

1. Introduction

The hypoxic state of a tumour is of key importance in its progression and response to treatment. The presence of hypoxia is associated with a poor prognosis, with hypoxic fraction inversely correlated to survival (Nordsmark *et al* 1996, Brizel *et al* 1997). It is also indicative of a poor response to both radiotherapy (Rofstad *et al* 2000) and chemotherapy.

The negative effect of hypoxia on radiotherapy is largely as a result of the treatment's reliance on oxygen to enhance the DNA damage for a given dose. The reduced response to chemotherapy is partly as a result of poor blood supply, but also because of cell-cycle inhibition. Many chemotherapeutics rely on the fact that tumour cells are actively dividing, therefore this reduces targetability.

Therefore, the assessment of the hypoxic state of a tumour is crucial in determining both an informed prognosis and the most prudent course of treatment. There are several means of measuring hypoxia, but the most common is by Eppendorf probe, where an electrode is inserted into the tumour, taking a series of pO_2 measurements along one or more tracks. Whilst such measurements are a direct representation of oxygen levels, there are numerous artefacts: values are only representative of a fraction of the tumour, measurements are averages of values in the local volume, and the invasive nature of the method can lead to tissue damage, potentially stimulating metastasis.

Molecular imaging methods such as positron emission tomography (PET), single photon emission computed tomography (SPECT), optical tomography and magnetic resonance imaging (MRI) present a solution to many of these problems, as they are non-invasive, and provide data across the whole tumour. It is important to realize however, that the limited resolving power of these techniques means that submicron determination of the location of compounds cannot be achieved. Only MRI provides submillimetre resolution and PET and SPECT are limited in the clinical scenario to $\sim$8 mm^3. Additionally, optical imaging suffers from depth constraints, SPECT from a low signal to noise ratio, and MRI from a lack of established hypoxia-specific tracers. PET is used extensively to estimate hypoxia, largely because of the wide availability of radiolabelled hypoxia-specific tracers such as fluorine-18 labelled fluoromisonidazole (Fmiso). For this reason, in this study we focus on PET as our molecular imaging modality.

Static studies, where activity is counted over a single fixed period, account for the majority of PET scans. It has been reported that tumour to muscle ratios of Fmiso activity are correlated with hypoxic fraction (Gagel *et al* 2004), and above a certain threshold, with poor prognosis. However, such single time point studies are prone to high variability (a threshold from one study may not correspond to a meaningful division in another study) due to the limited information available. In principle, data taken over multiple time points, in the form of tissue activity curves (TACs) provide a more robust indication of the presence of hypoxia. The shapes of these curves provide information on the degree of perfusion and vascularization, as well as the hypoxic fraction (Casciari *et al* 1995).

Determining the relationship between TAC shape and the underlying tumour physiology is of fundamental importance, as knowledge of the tumour environment may help determine the most sensible course of action. Standard techniques such as Patlak plots (Patlak *et al* 1983) and conventional compartment models (Sokoloff *et al* 1977, Blomqvist *et al* 1989) are limited in that they assume each compartment is a mathematical abstraction, independent of its location. This means that whilst movement between abstract compartments is considered, effects relating to the movement of tracer between physical locations, such as diffusion, are not. One notable exception decomposes Fmiso TACs into perfusion, diffusion and accumulation components (Thorwarth *et al* 2005). Despite this advance, it is difficult to use such models to

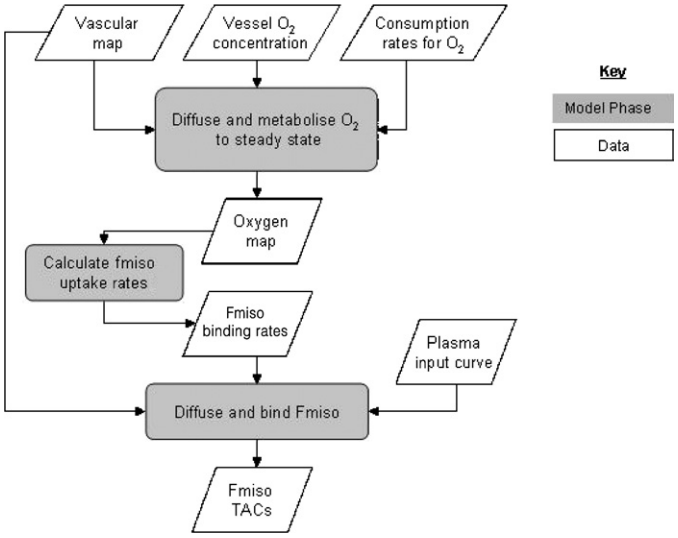

Figure 1. Schematic of the model: simulations are divided into three separate phases (in grey rectangles); diffusion and metabolism of O_2 to steady state, estimation of Fmiso binding rates and diffusion and binding of Fmiso. Each of these stages requires input and produces output. The relevant data for each stage are shown in white parallelograms.

answer questions regarding the consequences of perturbing the underlying physiology, since actual physical quantities, such as permeability and the local vascular supply, can be hidden in compound parameters.

It is the purpose of this paper to present a novel method for the simulation of realistic dynamic TACs, initially for the hypoxia-specific tracer Fmiso, although the modularity of the method enables straightforward application to other tracers. The organization of the paper is as follows: section 2 describes a computerized reaction–diffusion model, underpinned by the physiological principles of oxygen and tracer kinetics. At the heart of the model lies the representation of vasculature as a probability density function (PDF). The vasculature here is a 2D representation for simplicity, but the model can be extended to 3D. Section 3 outlines the conditions of simulations, while results are presented in section 4. Here, the utility of the model in reconciling underlying molecular-level physiology, with macroscale PET observations, is demonstrated. In section 5, the potential applications of the simulator are discussed, along with current limitations.

2. The model

Simulating the spatiotemporal distribution of a tracer from a measure of the vasculature is a multistep process. To minimize errors and to maximize the flexibility of the simulator, we adopted a modular approach, which can be validated at each step. A schematic of the model is shown in figure 1. The model has three distinct phases (shown in grey), each dependent on a number of inputs (shown in white).

First, for a given 2D map of vasculature, oxygen tension and consumption model, the steady-state distribution of O_2 tensions is obtained. From this map, the binding rates for Fmiso are estimated. Finally, given these binding rates, a plasma input curve and the original

vascular map, the spatiotemporal distribution of Fmiso is simulated. Each of these stages is now considered in more detail.

2.1. Vascular supply and oxygen tension

Hypoxia occurs as a result of a shortfall in the supply of oxygen relative to cellular consumption. Oxygen diffuses from the vasculature into the surrounding cells, where it is metabolized. If a cell is beyond the radius of diffusion (Thomlinson and Gray 1955), or if blood supply is compromised, cellular oxygenation will be subnormal. In tumours, hypoxia is often the result of a deficient vasculature, which is particularly chaotic and subject to leakiness (Secomb *et al* 1993).

The Krogh cylinder model (Krogh 1919) was the first model to consider the fate of oxygen along a blood vessel as a function of distance from the main supply. This model assumes a cylinder of tissue about a single blood vessel and is therefore not applicable for complex vascular networks. Alternatively, the system can be modelled using a reaction–diffusion model, such as that in equation (1):

$$\frac{\partial P_{[O_2]}(x, y, t)}{\partial t} = D_{O_2} \nabla^2 P_{[O_2]} - q_{\text{met}}\left(P_{[O_2]}\right) + F_s - F_{ls} \tag{1}$$

where $P_{[O_2]}$ is oxygen tension (mmHg) in tissue. Oxygen tension (mmHg) is used instead of concentration due to the direct relationship between O_2 concentration and partial pressure (Henry's law). D_{O_2} is the diffusion coefficient of oxygen ($cm^2\ s^{-1}$), q_{met} is the rate of oxygen metabolism as a function of oxygen tension (mmHg s^{-1}), F_s is the O_2 gain from the blood vessels and F_{ls} is loss of oxygen back to the capillaries. D_{O_2} is assumed to be spatially invariant. Transport is assumed to be dominated by diffusion, due to minimal convection caused by undeveloped intra-tumoral lymphatics. The constitutive equation for F_s is given by equation (2):

$$F_s = \frac{Pm_{O_2} S}{V}\left(\left(P_{[O_2]\text{vessel}} - P_{[O_2]}\right) \cdot R\right) \tag{2}$$

where Pm_{O_2} is the transvascular permeability of O_2 (ms^{-1}), $\frac{S}{V}$ is the surface area to volume ratio of the vasculature (m^{-1}), $P_{[O_2]\text{vessel}}$ is the oxygen tension in the supply vein and R is the vascular proportion. A venous supply is assumed, as it is often the case that tumour blood vessels often originate from this side of the vasculature (Vaupel *et al* 1989).

Parameter values are given in table 1. Estimated values for a single transvascular permeability coefficient are rare as, by Krogh's model, diffusion across the endothelium is a function of axial and radial diffusion. Fletcher and Schubert (1987) used Krogh's model to obtain a range of permeability values, which gave biologically feasible pO_2 histograms. The rate of oxygen (q_{met}) consumption is also somewhat contentious. The simplest form would be a single value for all tissues, as suggested by Warburg (1923) and employed previously by others (Pogue *et al* 2001). However, the assumption of homogeneous consumption is not accurate (Bingmann and Kolde 1982); a more likely strategy to conserve oxygen is to cap consumption in normoxic tissues and decrease it in areas of low oxygen tension. This phenomenon has been modelled using Michaelis–Menten kinetics with encouraging results (Bassom *et al* 1997, Daşu *et al* 2003). Equation (3) describes the Michaelis–Menten relationship between tissue oxygen tension and the rate of consumption, q_{met}:

$$q_{\text{met}} = q_{\max} \frac{P_{[O_2]}}{P_{[O_2]} + h} \tag{3}$$

where $q_{\max}$ is the maximum rate of oxygen consumption, and h is the oxygen tension at which q_{met} is half-maximal. Parameters for oxygen consumption are given in table 1.

Table 1. Baseline values of parameters used in simulation.

Parameters		Value	Reference
D_{O_2}	Diffusivity of oxygen	2×10^{-9} m^2 s^{-1}	Tannock (1972)
D_{Tr}	Diffusivity of misonidazole in multicellular membrane system	5.5×10^{-11} m^2 s^{-1}	Cowan (1996)
Pm_{O_2}	Permeability of tumour to oxygen	3×10^{-5}–3×10^{-4} m s^{-1}	Fletcher (1987)
Pm_{Tr}	Permeability of tumour to tracer	$(2.4–9.4) \times 10^{-5}$ m s^{-1}	Calculated from $Pm_{Tr} = \frac{K D_{Tr}}{\Delta x}$
q_{max}	Maximum rate of O_2 metabolism	15 mmHg s^{-1}	Daşu *et al* (2003)
h	O_2 tension at half maximal rate	2.5 mmHg s^{-1}	Daşu *et al* (2003)
S/V	Ratio of capillary surface area to volume	0.13–0.33 m^{-1}	Konerding *et al* (2001)
$S_{[O_2]}$	Venous O_2 tension	40 mmHg s^{-1}	Dewhirst (1992)
k_{on}	Rate of Fmiso binding in hypoxic cells (in terms of associated radioactivity)	10^{-4} kBq s^{-1}	Estimated from Thorwarth *et al* (2005) and Bruehlmeier *et al* (2004)
	Rate of Fmiso binding in normoxic cells (in terms of associated radioactivity)	2×10^{-5} kBq s^{-1}	Estimated from Gross *et al* (1995)
K	Partition coefficient of misonidazole	0.43	Workman (1980)
Δx	Width of capillary membrane	$0.2–1 \times 10^{-6}$ m	Wieser *et al* (2005)

The supply of oxygen to the tumour is dependent on the proximity, quality and density of the local vasculature. Clinically, the distribution of vessels is generally described as number per square millimetre (microvessel density; MVD). In a previous 2D simulation (Daşu *et al* 2003), tumour microvasculature was represented explicitly as individual vessels lying perpendicular to the plane of imaging. However, the orientation and position of vessels is highly heterogeneous.

Mindful of this, we propose an alternative representation of vasculature, denoted by R (equations (2) and (6)). In contrast to explicitly positioning a number of vessels perpendicular to the plane, corresponding to the MVD for that area (as in Daşu *et al* (2003)), we propose that the same *proportion* of tumour to be covered by vasculature, accounting for the uncertainty in position.

As a specific example, given a normally-distributed MVD distribution, m, with known mean and variance, a single value which will determine the microvessel density of the vascular map, is selected at random. Assuming a vessel radius, r, of 10 μm (Konerding *et al* 2001), and that vessels run perpendicular to the 2D plane, the proportion, p, of the vascular map covered by vessels is estimated using equation (4):

$$p = \frac{\left(\mathrm{MVD}_{\mathrm{ma}} \times \pi r^2\right)}{\mathrm{ma}} \tag{4}$$

where $\mathrm{MVD}_{\mathrm{ma}}$ represents the MVD for the area of the vascular map (ma). The vascular map is then generated by randomly assigning vessel or not vessel (one or zero), for each grid point, with the probability of a vessel equal to p.

Given the probabilistic spatial distribution of vessels in which the vessels are orthogonal to the plane, we next model their random orientations relative to the image plane. We reasonably assume that the random orientation is shift invariant and that the process is linear, that is to say, orientation can be modelled as a convolution applied to the spatial distribution. A formal analysis of the convolution kernel is not straightforward, but it is evidently monomodal, and falls to zero at some distance. Our analysis suggests that a portion of a cosine between $-\pi/2$ and $\pi/2$ is a good approximation to the convolution kernel, and this is borne out in a number

of simulations that we have done. Here we apply a 3×3 convolution kernel to the vascular map.

Prior to convolution with the orientation operator (cosine), the number of vessels within the whole grid follows a binomial distribution $X \sim \mathrm{Bin}(n,p)$ where n is the number of grid points. The variance of the proportion of vascularized grid points within the vascular map is the sum of the variances of the MVD distribution and sampling from the binomial distribution. The variance of vascularized grid points is thus always higher than the true variance of microvessel densities. As the grid size approaches infinity, the sampling variation effectively reduces to zero, and the distribution of vascular maps represents the true MVD distribution. However, even on a grid size of 100×100, the contribution of the binomial sampling to the total variance is small (a third) compared to the contribution from the MVD variance.

Several consequences are associated with the assumptions outlined above. The assumption of vessel perpendicularity improves ease of calculation, but is likely to lead to an underestimation of vascularity. MVDs are estimated by counting the presence or absence of a vessel in a plane of view, regardless of orientation, thus a single vessel running parallel to the plane is likely to occupy a greater area than the vessel cross-section. Here the 3×3 cosine convolution increases the vessel coverage $\sim \times 4$. Our analysis of microvessel staining (results not published) showed that the mean extent of a single vessel in a 2D plane is approximately four 10×10 μm pixels, thus a natural condition for the vascular maps is that grid point dimensions be 10×10 μm.

Assuming that microvessel densities are distributed normally across tumours is not wholly accurate, as negative densities are impossible. However, given that 95% of normally distributed values will lie within two standard deviations of the mean, and that published samples of microvessel densities (Tae *et al* 2000, Erovic *et al* 2005) have standard deviations less than one third the magnitude of the mean, misrepresentation of the distribution due to sampling using this method is unlikely.

2.2. *Fmiso binding and distribution*

Cellular binding of Fmiso occurs as a result of the activity of nitroreductases, which transfer an electron to the nitro group of Fmiso. Under normoxic conditions, oxygen, having a higher affinity for electrons, reverses this reaction. In the absence of oxygen, Fmiso can become further reduced, forming covalent bonds with cellular macromolecules. This binding occurs at low levels under normoxic conditions, increasing nonlinearly as oxygen tension decreases (Gross *et al* 1995).

The pharmacokinetics of the unlabelled misonidazole have been well described (Workman 1980). To date, the uptake of Fmiso has generally been described using compartment models (Casciari *et al* 1995, Bruehlmeier *et al* 2004), the shortcomings of which have been noted earlier. The use of reaction–diffusion or convection–reaction–diffusion models to describe the distribution of other drugs in tumours is well documented, from Baxter and Jains' description of the distribution of macromolecules in a radially symmetric tumour (Baxter and Jain 1989, 1990, 1991), to the delivery of the misonidazole analogue, etanidazole, to brain tumours (Tan *et al* 2003). Following the same principles, the spatiotemporal distributions of both free and bound Fmiso are modelled here using equation (5):

$$\begin{aligned} \frac{\partial Tr_{\mathrm{free}}(x,y,t)}{\partial t} &= D_{\mathrm{Tr}}\nabla^2 Tr_{\mathrm{free}} - k_{\mathrm{on}} Tr_{\mathrm{free}} + k_{\mathrm{off}} Tr_{\mathrm{bound}} + G_{\mathrm{s}} - G_{\mathrm{ls}} \\ \frac{\partial Tr_{\mathrm{bound}}}{\partial t}(x,y,t) &= k_{\mathrm{on}} Tr_{\mathrm{free}} - k_{\mathrm{off}} Tr_{\mathrm{bound}} \end{aligned} \tag{5}$$

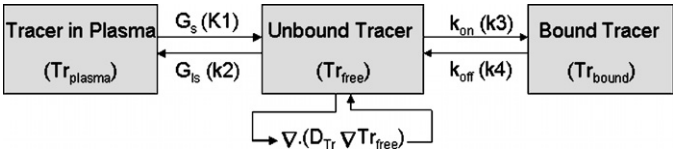

Figure 2. Relationship between standard two-compartment model and equation (4). Movement between plasma, free and bounds states is governed by four parameters equivalent to the $K1$, $k2$, $k3$ and $k4$ seen in conventional compartment models. The additional component is a diffusive rate constant which links to the spatial domain.

where Tr_{free} is the concentration of free tracer in cells and the interstitium, D_{Tr} is the diffusion coefficient of Fmiso through the interstitium, k_{on} and k_{off} are the 'on and off' rates of Fmiso binding, Tr_{bound} is the concentration of bound tracer in cells, Tr_{plasma} is the concentration of tracer in the plasma, G_{s} is the net gain of tracer from the capillary and G_{ls} is the loss of tracer back to the capillaries. D_{Tr} is assumed to be spatially invariant. Due to an undeveloped lymphatic system, it is assumed that little or no convection occurs. G_{s} is given by equation (6):

$$G_{\text{s}} = \frac{Pm_{\text{Tr}}S}{V}(Tr_{\text{plasma}} - Tr_{\text{free}}) \cdot R \tag{6}$$

where R is the vascular proportion, Tr_{plasma} is the concentration of tracer in the plasma (from a plasma input function), and Pm_{Tr} is the transvascular permeability of the vessel to the tracer. The rate of Fmiso binding, k_{on}, has been estimated by numerous authors (Rasey *et al* 2000, Bruehlmeier *et al* 2004), from compartment model fits, with values differing significantly. As previously, k_{off} is assumed to be zero over the time course of a conventional PET scan (Thorwarth *et al* 2005).

Figure 2 demonstrates how the model described in this section relates to a two-compartment reversible binding model (Sokoloff *et al* 1977). Movement between plasma, free and bounds states is governed by four parameters, which are equivalent to the rate constants $K1$, $k2$, $k3$ and $k4$ seen in conventional compartment models (e.g., Bruehlmeier *et al* (2004)). The additional component considered is a diffusive rate constant, which effectively links the locationless compartments to the spatial domain.

3. Methods

3.1. Simulation conditions

All simulations were coded in Matlab (Matlab 2005), in 2D, using finite-difference methods. MVD distributions known to produce hypoxia were estimated from empirical data (van Laarhoven *et al* 2006) where a single vessel was defined as a connected series of positively-stained pixels. MVDs were distributed normally, $\mu = 58.1$ vessels mm^{-2}, $\sigma = 9.5$.

Oxygen tension maps at steady state were achieved numerically, by solving equation (1) to steady state. Assumption of steady state would appear a reasonable starting supposition, as capillary pO_2 is less subject to the fluctuations caused by the heartbeat than arterial pO_2 due to elastic recoil in the arterial walls and the structural changes associated with angiogenesis happen over a timescale longer than that with which we are concerned (Hansen-Algenstaedt *et al* 2005). However, as a result of vessels temporarily shutting or collapsing due to the pressure from surrounding cells, the supply is both temporally and spatially heterogeneous,

with pulsatile flow still discernible at the microvascular level. For this series of experiments, we have not considered this flow heterogeneity, although the vascular model could be adapted. At each time step, the pO_2 or tracer concentration is incremented, according to the plasma concentration weighted by the local vascularity measure R, prior to diffusion taking place. The net diffusion at the tumour edge was set to be zero (Neumann boundary condition).

Parameters for Fmiso binding were set according to pixelwise oxygen tensions. For each set of initial conditions, the spatiotemporal distribution of the tracer was simulated for 60 min, using a plasma activity curve as input (provided by Matthias Bruehlmeier, Cantonal Hospital, Switzerland) to equation (4). Using a plasma activity curve as input to the model necessitates some assumptions, as the activity observed is only representative of the concentration of Fmiso, which itself diffuses and is bound. The activity observed must be closely related to Fmiso concentrations, i.e. the signal should largely derive from the unchanged parent compound, and not metabolites. This is true for Fmiso over the time course of a normal PET scan, where $>90\%$ of the compound remains unchanged after 90 min (personal correspondence with Matthias Bruehlmeier). Furthermore, it is essential that the input function is decay corrected, otherwise latter time points become unrepresentative of Fmiso concentrations.

3.2. Data evaluation

3.2.1. Oxygen distribution generation. The shape and extent of hypoxic islands in ten simulated datasets (oxygen maps generated from MVD described above) were compared quantitatively to a clinical dataset (van Laarhoven *et al* 2006). An elongation index for hypoxia (EIH), defined previously (Ljungkvist *et al* 2002), was calculated to determine the similarity in shape between datasets. EIH is given by A/B, where A is the longest and B is the shortest axis of each hypoxic area. The metric for extent was defined as the hypoxic fraction, given by the area of hypoxic tissue ($pO_2 < 5$ mmHg) as a percentage of the total tissue area. Similarity was assessed using a two-sample unpaired t-test.

To assess the effect of convolving the vascular map with a cosine, a vascular map was generated using equation (4) and was either convolved with the orientation operator or multiplied by a factor of 4, corresponding to the increase in magnitude of supply generated by the convolution (section 2.1).

3.2.2. Fmiso TAC generation. TACs were generated from oxygen maps as described above. The relationship between underlying vascular PDF and TAC morphology was assessed by describing representative TACs in terms of their local PDF. Finally, two parameters, the distance to the nearest vessel and Fmiso diffusion coefficient, were altered systematically (10 to 80 μm and 1×10^{-13} to 1×10^{-10} cm^2 s^{-1}, respectively) for a vascular map comprising a single vessel, with the resulting changes in TAC morphology evaluated qualitatively.

4. Results

4.1. Vascular representations

Figure 3 shows vascular maps at two scales; 1 mm to demonstrate fine scale resolution (a) and 5 mm representing a coarser scale (b). The two representations demonstrate the effect of the probabilistic mechanism of tumour vessel generation, i.e. at a coarse scale resolution, vasculature can appear largely homogeneous, with its true chaotic nature, including the spatial separation sufficient for islands of hypoxia to form, becoming more apparent at higher resolution.

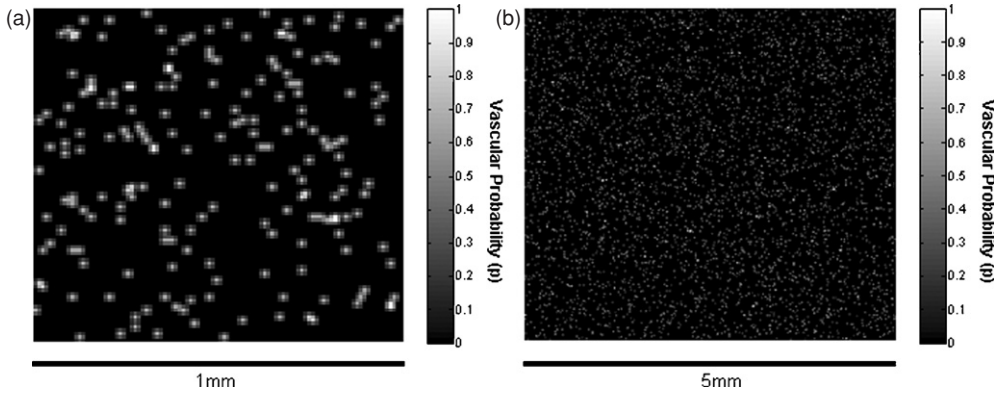

Figure 3. Vascularity maps sampled from an MVD distribution (58.1 ± 9.6 vessels mm^{-2}), at different scales: (a) 1 mm, (b) 5 mm.

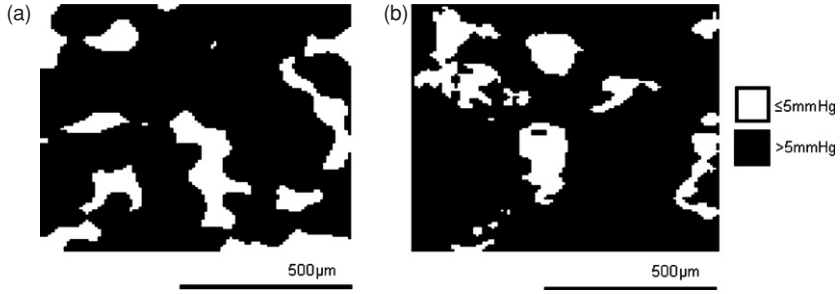

Figure 4. Comparison of hypoxic island distributions between simulated and real data (provided by van Laarhoven *et al* (2006)). Note that these distributions derive from different vasculature. Simulated data (a) show potential hypoxic staining in white. Real pimonidazole staining (b) is shown in white[1]. Whilst staining is not identical, the size and distribution of islands, determined using an elongation index and the hypoxic fraction respectively, are alike. $S_{[O_2]} = 40$ mmHg, $Pm_{O2} = 6 \times 10^{-5}$ m s^{-1}. Scale bar = 500 μm.

4.2. Distribution of hypoxic islands

Figure 4(a) shows a 1 mm^2 simulated hypoxic map, generated from the vascular map in figure 3(a). Figure 4(b) is a 1 mm^2 section, taken from a slice of hypoxic tissue (van Laarhoven *et al* 2006) stained with pimonidazole, a marker similar in both structure and distribution to Fmiso (Arteel *et al* 1995). The tissue section, taken from a clinical image of ∼30 mm^2, suffered from pixelation upon scaling; hence for visualization, median filtering (3 × 3) has been applied. Despite deriving from different vasculature, there is a similarity between the size and distribution of hypoxic islands, suggesting that the vascular PDF models microvasculature well. The hypoxic fractions are similar (real: 18.14 ± 4.9 simulated: 18.49 ± 8.8, $p < 0.1$, $n = 10$) as are the EIHs for the two datasets (real: 2.6 ± 1 simulated: 2.5 ± 0.78, $p < 0.1$ $n = 10$). Islands of hypoxia can be classified as 'ribbon-like', 'patchy' or a mixture of both (Ljungkvist *et al* 2002). The hypoxic islands from the clinical dataset here are

[1] Reprinted from van Laarhoven *et al*, copyright 2006, with permission from Elsevier.

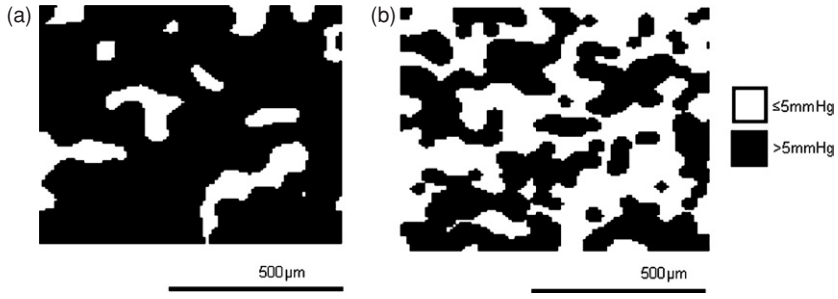

Figure 5. Comparison of hypoxic island distributions for the same initial vascular map (a) convolved with orientation convolution operator and (b) without convolution, scaled by the same magnitude (×4). The hypoxic fraction is greatly reduced (threefold) with the convolution operator. $S_{[O_2]} = 40$ mmHg, $Pm_{O2} = 6 \times 10^{-5}$ m s^{-1}. Scale bar = 500 μm.

examples of patchy/elongated islands, whereas the simulated islands appear to exhibit all of the classifications.

4.3. Significance of orientation convolution

The effect of the convolution operation is highlighted in figure 5, which shows hypoxic maps generated from the same initial vascular map with (a) and without (b) the convolution operator. Using the orientation convolution produces individual hypoxic islands, similar to those seen in the literature. In the absence of the convolution, the islands merge together to form long continuous regions of hypoxia. The associated increase in hypoxic fraction is threefold.

4.4. Tissue activity curves

Simulated TACs, generated using patient plasma data, are shown in figure 6(a). These curves represent both well-perfused and diffusion-limited tissue. The shapes of the TACs are similar to those obtained empirically, where an exponential washout follows an initial peak, which either follows plasma levels, or is replaced by a slow but definite take up, representative of hypoxic tissue. The effective binding rate of Fmiso that best fit the slopes observed by others (Bruehlmeier *et al* 2004, Thorwarth *et al* 2005) is $\sim 10^{-4}$ s^{-1} for hypoxic tissue, lower than previously estimated from compartment models.

4.4.1. Relationship with underlying physiology. The relationship between TACs and the underlying vascular PDF is highlighted in figure 6 (each pixel is equivalent to 10 μm). The central pixel of each vascular PDF corresponds to the source of one of the TACs in figure 6(a) while the surrounding pixels describe the local PDF. Figure 6(b) represents a well-perfused region, and as such, the respective TAC has an initial perfusion peak and no subsequent uptake. Figure 6(c) represents a poorly-perfused region, with diffusion-limited hypoxia. This is supported by the reduction in perfusion peak in the corresponding TAC and the presence of an accumulation slope.

Simulations also prove useful for investigating the potential effects of alterations to physiology on observations. As part of this, confounding physiologies may be brought to light, which although structurally different, may result in similar TAC shapes. This is

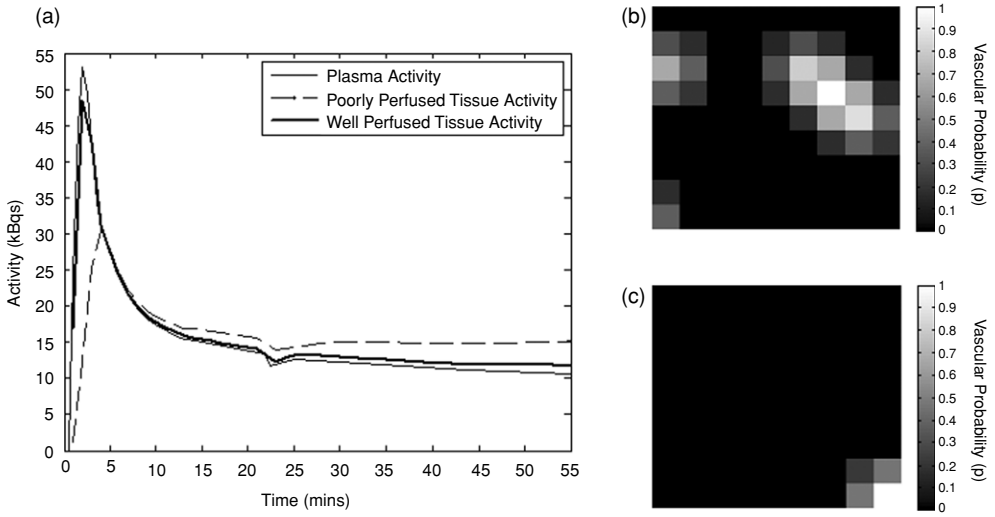

Figure 6. Example tissue activity curves for Fmiso. (a) Example TACs shown with plasma input function. ((b) and (c)) Underlying vascular PDF corresponding to TACs in (a). Dark pixels indicate a low vascular probability, whilst lighter pixels indicate increasing probability of vasculature. Scale bar = 50 μm. Local PDF representing well perfused tissue (b) and local PDF representing poorly perfused tissue in (c).

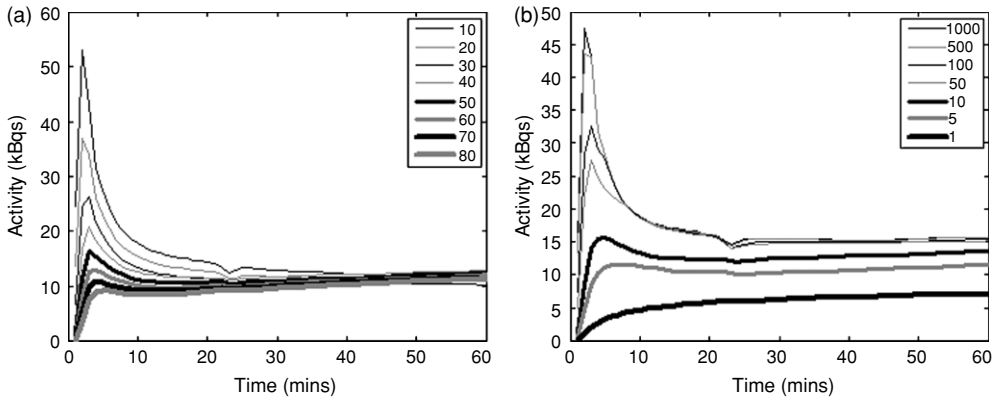

Figure 7. Consequences of modifying the diffusion distance and diffusion coefficient for the tracer. Diffusion distance varied from 0 to 80 μm from a single vessel. Diffusion coefficient varied from 1×10^{-10} m^2 s^{-1} decreasing to 1×10^{-13} m^2 s^{-1}. (a) Increasing the distance that the tracer must diffuse through the interstitium before it reaches tissue decreases the perfusion peak (scale: μm). (b) Decreasing the diffusion coefficient of the tracer (D_{Tr}) decreases the perfusion peak, with activity solely deriving from hypoxia-related binding (scale: $\times 10^{-13}$ m^2 s^{-1}).

particularly crucial when considering treatment. To demonstrate this, the distance of tissue from a single vascular supply (a 30 μm diameter vessel) and the diffusion coefficient of Fmiso, D_{Tr}, were systematically altered, with the respective results shown in figure 7. D_{Tr} may either be representative of a new drug or, indirectly, the local tissue density, which is likely to have consequences for drug delivery.

As the distance between tissue and the nearest vessel increases, so the peak in perfusion decreases in magnitude and moves towards a later time point. The change in TAC shape is a combination of the decreasing oxygen availability and the increasing distance for tracer diffusion; the former leading to hypoxia and increased binding, the latter leading to a reduction in perfusion. Figure 7(a) shows the transition from normoxic to hypoxic tissue, as the perfusion dominated TAC is slowly replaced by the diffusion-limited equivalent. Changing the diffusion coefficient has a similar initial effect, as decreasing D_{Tr} leads to a progressive reduction in initial peak size (figure 7(b)). The latter slope of the curve is largely unaffected however, as the degree of hypoxia remains unchanged. Instead, a lower diffusion coefficient is associated with lower relative levels of binding. This may not be significantly different when compared to background, however and, with the addition of noise, these curves stemming from different physiologies may lead to a similar assessment.

5. Discussion

We have combined the standard compartment model (Sokoloff *et al* 1977), frequently used in dynamic PET studies, with a reaction–diffusion equation to better model the molecular dynamics of tracer distributions. Simulation of tracer spatiotemporal distributions has the potential to answer a range of questions, as it enables the investigation of relationships between image data and molecular processes, prior to empirical studies.

The vascular PDF underpinning the simulations appears to represent true microvasculature well, as the correspondence of hypoxic island shape and distribution between real and simulated data suggests. The effect of the convolution operation introduced to include a measure of vessel orientation is significant. The associated threefold reduction in hypoxic fraction better matches empirical observations. This would suggest that the extent of the vasculature (area occupied) is of relatively greater significance than the magnitude of the supply in maintaining adequate tissue oxygenation, and that the consideration of orientation is important.

Simulated TACs demonstrate the general trends of empirical data, with activity in well-perfused tissue following plasma levels in early stages, and binding only becoming apparent at a later stage. In structurally hypoxic tissue (further away from the vascular supply), the initial part of the curve is dominated by a more gradual increase in activity, followed by the same accumulation slope. As suggested by Thorwarth *et al* (2005), whilst the late slope of the curve indicates the presence of hypoxia, the initial section points to the local vascular supply. By gradually changing the proximity of tissue to the vasculature, we can see the shift from well-perfused to avascular regions in process.

5.1. Potential applications

One of the key complications of parameterizing compartment models derives from tissue heterogeneity. TACs obtained for a single voxel are the sum of different underlying tissue components (e.g. vasculature, hypoxic and normoxic tissue). As compartment model parameters are derived nonlinearly, estimation of the hypoxic fraction may be biased, for example. The model presented here, a combination of oxygen and Fmiso dynamics underpinned by a heterogeneous vascular representation, enables a detailed investigation of the effects of this heterogeneity on observable TACs.

As a first approach, we have parameterized the model to describe only the spatiotemporal distribution of Fmiso, dependent on underlying oxygen tensions. In terms of explaining the total physiology of a cancer however, other tracers such as FDG, FLT and ^{15}O-H_2O can provide complementary information about metabolism, cell division and perfusion, and there

is a growing argument that information from multiple-tracer studies should be combined (Bruehlmeier *et al* 2004, Lehtio *et al* 2004). Due to its inherent modularity, our model is highly adaptable and offers the opportunity to investigate the fate of coadministered tracers in a simulation environment, with an eye to devising optimal procedures.

We have demonstrated that simulations are useful in assessing the change in TAC morphology, in response to altered physiology. A natural progression would be to assess directly these changes via PET studies.

5.2. Limitations

The model as it stands does not describe the effects of interstitial pressure. Our tumour representation is a semi-closed system where oxygen and Fmiso can enter, but not leave (unless by metabolism), which is highly unrealistic. As fluid enters the tumour by convection, interstitial pressure increases, exerting an outwards force.

Another limitation is that the model allows the same potential maximum value of oxygen for all microvessels, regardless of their distance from the periphery. The Krogh cylinder model (Krogh 1919) accounts for the loss of oxygen along a single capillary and it would be pertinent to incorporate some form of this, as the model presented here is likely to underestimate the levels of hypoxia by incorrectly assuming zero loss of oxygen tension. Other physiological quantities such as pH, interstitial pressure and lymphatic drainage may contribute to the spatiotemporal distribution of the tracer. It is our intention that these factors be considered as potential model incorporations.

The vascular model samples randomly from a distribution, so does not capture the long range correlations, i.e. continuous or parallel vessels networks, observed empirically. However, the incorporation of orientation uncertainty is a step towards a more comprehensive vascular representation.

6. Conclusion

This paper presents a novel tool for the simulation of realistic dynamic tissue activity curves, for the hypoxia-specific tracer Fmiso, underpinned by a realistic model of vasculature. The results presented here show that the output from the tool provides a qualitative likeness of the kinetics of Fmiso. The most exciting aspect however is the ability to make quantitative predictions of how altering physiological parameters affects macroscale observations.

Acknowledgments

We would like to thank Dr Matthias Bruehlmeier (Cantonal Hospital, Switzerland), Daniela Thorwarth (Tubingen University), Dr Hanneke van Laarhoven (University Medical Center Nijmegen), and Drs Tiina Roose and Matt Kelly (University of Oxford), for provision of data and insightful discussion. We also wish to acknowledge the significant contribution to our work made by the anonymous reviewer. The work was supported by a grant from the Interdisciplinary Research Consortium in Medical Images and Signals, and by the EPSRC and MRC.

References

Arteel G E, Thurman R G, Yates J M and Raleigh J A 1995 Evidence that hypoxia markers detect oxygen gradients in liver: pimonidazole and retrograde perfusion of rat liver *Br. J. Cancer* **72** 889–95

Bassom A P, Ilchmann A and Voss H 1997 Oxygen diffusion in tissue preparations with Michaelis–Menten kinetics *J. Theor. Biol.* **185** 119–27

Baxter L T and Jain R K 1989 Transport of fluid and macromolecules in tumors: I. Role of interstitial pressure and convection *Microvasc. Res.* **37** 77–104

Baxter L T and Jain R K 1990 Transport of fluid and macromolecules in tumors: II. Role of heterogeneous perfusion and lymphatics *Microvasc. Res.* **40** 246–63

Baxter L T and Jain R K 1991 Transport of fluid and macromolecules in tumors: III. Role of binding and metabolism. *Microvasc. Res* **41** 5–23

Bingmann D and Kolde G 1982 PO_2-profiles in hippocampal slices of the guinea pig *Exp. Brain Res.* **48** 89–96

Blomqvist G, Pauli S, Farde L, Ericksson L, Persson A and Halldin C 1989 Clinical research and clinical diagnosis *Dynamic Models of Reversible Ligand Binding* ed C Beckers, A Goffinet and A Bol (New York: Kluwer)

Brizel D M, Sibley G S, Prosnitz L R, Scher R L and Dewhirst M W 1997 Tumour hypoxia adversely affects the prognosis of carcinoma of the head and neck *Int. J. Radiat. Oncol. Biol. Phys.* **38** 285–9

Bruehlmeier M, Roelcke U, Schubiger P A and Ametamey S M 2004 Assessment of hypoxia and perfusion in human brain tumors using PET with 18F-fluoromisonidazole and 15O–H_2O *J. Nucl. Med.* **45** 1851–9

Casciari J J, Graham M M and Rasey J S 1995 A modeling approach for quantifying tumour hypoxia with [F-18]fluoromisonidazole PET time-activity data *Med. Phys.* **22** 1127—39

Cowan D S, Hicks K O and Wilson W R 1996 Multicellular membranes as an *in vitro* model for extravascular diffusion in tumours *Br. J. Cancer Suppl.* **27** S28–31

Daşu A, Toma-Daşu I and Karlsson M 2003 Theoretical simulation of tumour oxygenation and results from acute and chronic hypoxia *Phys. Med. Biol.* **48** 2829–42

Erovic B M, Neuchrist C, Berger U, El-Rabadi K and Burian M 2005 Quantitation of microvessel density in squamous cell carcinoma of the head and neck by computer-aided image analysis *Wien. Klin. Wochenschr.* **117** 53–7

Fletcher J E and Schubert R W 1987 Axial diffusion and wall permeability effects in perfused capillary-tissue structures *Biosystems* **20** 153–74

Gagel B *et al* 2004 pO(2) Polarography versus positron emission tomography ([(18)F] fluoromisonidazole, [(18)F]-2-fluoro-2'-deoxyglucose): an appraisal of radiotherapeutically relevant hypoxia *Strahlenther. Onkol.* **180** 616–22

Gross M W, Karbach U, Groebe K, Franko A J and Mueller-Klieser W 1995 Calibration of misonidazole labeling by simultaneous measurement of oxygen tension and labeling density in multicellular spheroids *Int. J. Cancer* **61** 567–73

Hansen-Algenstaedt N *et al* 2005 Long-term observation reveals time-course-dependent characteristics of tumour vascularisation *Eur. J. Cancer* **41** 1073–85

Haustermans K, Hofland I, Van de Pavert L, Geboes K, Varia M, Raleigh J and Begg A C 2000 Diffusion limited hypoxia estimated by vascular image analysis: comparison with pimonidazole staining in human tumors *Radiother. Oncol.* **55** 325–33

Konerding M A, Fait E and Gaumann A 2001 3D microvascular architecture of pre-cancerous lesions and invasive carcinomas of the colon *Br. J. Cancer* **84** 1354–62

Krogh A 1919 The number and distribution of capillaries in muscles with calculations of the oxygen pressure necessary for supplying tissue *J. Physiol. (London)* **52** 409–15

Lehtio K, Eskola O, Viljanen T, Oikonen V, Gronroos T, Sillanmaki L, Grenman R and Minn H 2004 Imaging perfusion and hypoxia with PET to predict radiotherapy response in head-and-neck cancer *Int. J. Radiat. Oncol. Biol. Phys.* **59** 971–82

Ljungkvist A S, Bussink J, Rijken P F, Kaanders J H, Van Der Kogel A J and Denekamp J 2002 Vascular architecture, hypoxia, and proliferation in first-generation xenografts of human head-and-neck squamous cell carcinomas *Int. J. Radiat. Oncol. Biol. Phys.* **54** 215–28

MATLAB version 7.1.0. 2005 (Natick, MA: The MathWorks Inc.)

Nordsmark M, Overgaard M and Overgaard J 1996 Pretreatment oxygenation predicts radiation response in advanced squamous cell carcinoma of the head and neck *Radiother. Oncol.* **41** 31–9

Patlak CS, Blasberg RG and Fenstermacher JD 1983 Graphical evaluation of blood-to-brain transfer constants from multiple-time uptake data *J. Cereb. Blood Flow Metab.* **3** 1–7

Pogue B W, Paulsen K D, O'Hara J A, Wilmot C M and Swartz H M 2001 Estimation of oxygen distribution in RIF-1 tumors by diffusion model-based interpretation of pimonidazole hypoxia and eppendorf measurements *Radiat. Res.* **155** 15–25

Rasey J S, Casciari J J, Hofstrand P D, Muzi M, Graham M M and Chin L K 2000 Determining hypoxic fraction in a rat glioma by uptake of radiolabelled fluoromisonidazole *Radiat. Res.* **153** 84–92

Rofstad E K, Sundfor K, Lyng H and Trope C G 2000 Hypoxia-induced treatment failure in advanced squamous cell carcinoma of the uterine cervix is primarily due to hypoxia-induced radiation resistance rather than hypoxia-induced metastasis *Br. J. Cancer* **83** 354–9

Secomb T W, Hsu R, Dewhirst M W, Klitzman B and Gross J F 1993 Analysis of oxygen transport to tumour tissue by microvascular networks *Int. J. Radiat. Oncol. Biol. Phys.* **25** 481–9

Sokoloff L, Reivich M, Kennedy C, DesRosiers M H, Patlak C S, Pettigrew K D, Sakurada O and Shinohara M 1977 The 14C-deoxyglucose method for the measurement of local cerebral glucose utilisation: theory, procedure and normal values in the conscious and anaesthetized albino rat *J. Neurochem.* **28** 897–916

Tae K, El-Naggar A K, Yoo E, Feng F, Lee J J, Hong W K, Hittelman W N and Shin D M 2000 Expression of vascular endothelial growth factor and microvessel density in head and neck tumorigenesis *Clin. Cancer Res.* **6** 2821–28

Tan W H, Wang F, Lee T and Wang C H 2003 Computer simulation of the delivery of etanidazole to brain tumour from PLGA wafers: comparison between linear and double burst release systems *Biotechnol. Bioeng.* **82** 278–88

Tannock I F 1972 Oxygen diffusion and the distribution of cellular radiosensitivity in tumours *Br. J. Radiol.* **45** 515–24

Thorwarth D, Eschmann S M, Paulsen F and Alber M 2005 A kinetic model for dynamic [18F]-Fmiso PET data to analyse tumour hypoxia *Phys. Med. Biol.* **50** 2209–24

Thomlinson R H and Gray L H 1955 The histological structure of some human lung cancers and the possible implications for radiotherapy *Br. J. Cancer* **9** 539–49

van Laarhoven H W, Kaanders J H, Lok J, Peeters W J, Rijken P F, Wiering B, Ruers T J, Punt C J, Heerschap A and Van Der Kogel A J 2006 Hypoxia in relation to vasculature and proliferation in liver metastases in patients with colorectal cancer *Int. J. Radiat. Oncol. Biol. Phys.* **64** 473–82

Vaupel P, Kallinowski F and Okunieff P 1989 Blood flow, oxygen and nutrient supply, and metabolic microenvironment of human tumors: a review *Cancer Res.* **49** 6449–65

Warburg O 1923 Versuche am überlebenden Karzi-Nomgewebe *Biochem. Z.* **142** 317–33

Wieser E, Strohmeyer D, Rogatsch H, Horninger W, Bartsch G and Debbage P 2005 Access of tumour-derived macromolecules and cells to the blood: an electron microscopical study of structural barriers in microvessel clusters in highly malignant primary prostate carcinomas *Prostate* **62** 123–32

Workman P 1980 Pharmacokinetics of hypoxic cell radiosensitizers: a review *Cancer Clin. Trials* **3** 237–51

Yeh S H, Liu R S, Wu L C, Yang D J, Yen S H, Chang C W, Yu T W, Chou K L and Chen K Y 1996 Fluorine-18 fluoromisonidazole tumour to muscle retention ratio for the detection of hypoxia in nasopharyngeal carcinoma *Eur. J. Nucl. Med.* **23** 1378–83